ARTICLE

Adaptive Noise Cancellation Algorithms Implemented onto FPGA-Based Electrical Impedance Tomography System

Marlin R Baidillah[*]   **Zengfeng Gao**   **Al-Amin S Iman**   **Masahiro Takei**

Graduate School of Science & Engineering, Dept. Mechanical Eng., Div. Fundamental Eng., Chiba University, Chiba 263-8522, Japan

ARTICLE INFO	ABSTRACT

Electrical Impedance Tomography (EIT) as a non-invasive of electrical conductivity imaging method commonly employs the stationary-coefficient based filters (such as FFT) in order to remove the noise signal. In the practical applications, the stationary-coefficient based filters fail to remove the time-varying random noise which leads to the lack of impedance measurement sensitivity. In this paper, the implementation of adaptive noise cancellation (ANC) algorithms which are Least Mean Square (LMS) and Normalized Least Mean Square (NLMS) filters onto Field Programmable Gate Array (FPGA)-based EIT system is proposed in order to eliminate the time-varying random noise signal. The proposed method was evaluated through experimental studies with biomaterial phantom. The reconstructed EIT images with NLMS is better than the images with LMS by amplitude response $AR = 12.5\%$, position error $PE = 200\%$, resolution $RES = 33\%$, and shape deformation $SD = 66\%$. Moreover, the Analog-to-Digital Converter (ADC) performances of power spectral density (PSD) and the effective number of bit $ENOB$ with NLMS is higher than the performances with LMS by $S_l = 5.7\%$ and $ENOB = 15.4\%$. The results showed that implementing ANC algorithms onto FPGA-based EIT system shows significantly more accurate image reconstruction as compared without ANC algorithms implementation.

1. Introduction

Electrical Impedance Tomography (EIT) employs multi-frequency impedance measurement within several electrodes that attached on the periphery of the dielectric object in order to reconstruct the conductivity distribution. This conductivity distribution represents a useful meaning that varies with the application of EIT such as an anomaly functional biological tissues in the medical imaging applications or a multiphase flow visualization in the process imaging applications. In terms of EIT hardware design type, Field Programmable Gate Array (FPGA)-based systems are continuously gaining interest as compared to programmable digital signal processor (PDSP)-based systems due to their flexibility and higher bandwidth. Moreover, the FPGA-based EIT system allows us to take high-speed impedance measurement in a multi-electrode sensor with a sweep frequency which suitable with the required performance

Corresponding Author:
Marlin R Baidillah,
Graduate School of Science & Engineering, Dept. Mechanical Eng., Div. Fundamental Eng., Chiba University, Chiba 263-8522, Japan;
Email: mr.baidillah@c-techlabs.com

of the EIT system for medical imaging such as cell sensing in micro-channel [1], thrombus formation in blood flow [2], and for process imaging such as multi-phase flow [3], characterizations of Lithium-Ion battery [4].

In practical EIT applications, the noise signal sources mainly behave as a time-varying random noise, which is difficult to overcome by the stationary-coefficient based filters [5-9]. In FPGA-based EIT system, the readout chain in the architecture of noise cancellation, the electronic circuit components, and the electronic circuit noise signal levels synergies each other to achieve the SNR of EIT system [10,11] Consequently, the architecture of noise cancellation of FPGA-based EIT system should be considered in advance, because of insufficiently high signal-to-noise SNR in EIT system leads to the lack of impedance measurement sensitivity due to the time-varying random noise [12,13]. The challenge in the development of FPGA-based EIT system for medical imaging is to achieve an acceptable SNR level of as low as 90 dB [14] by finding a matching the architecture of noise cancellation and the high sensitivity detection.

In order to eliminate the noise signal caused by a time-varying random noise in the FPGA-based EIT system, one of the alternatives is by employing the adaptive noise cancellation (ANC) that can be integrated directly onto FPGA [15]. As compared with stationary-coefficient based filters such as FFT filters, using ANC provides a more appropriate application in the case of statistical parameters of signals change over time [16]. Previous investigators of FPGA-based EIT system [17-23] did not consider the ANC and only applied with a specific architecture of noise cancellation based-on stationary-coefficient based filters by assuming there is no temporal variant environment (leads to the time-varying random noise).
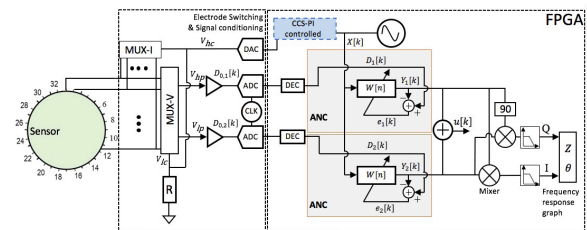
The implementation of ANC onto FPGA-based EIT system is used to discriminate between the sensing signal D_i and the noise signal h which depends on the electronics circuit design and frequently leads to a different architecture of noise cancellation [24-26]. The ANC automatically adjusts the filter transfer function based on an optimization algorithm. In digital signal processing fields, two different ANC algorithms are popular in the FPGA-based system, i.e., the Least Mean Square (LMS) and the Normalized the Least Mean Square (NLMS). The LMS finds the transfer function coefficients by calculating the least mean squares of the error signal between the output signal Y_i and the sensing signal D_i itself [27]. On the other hand, the NLMS is developed to overcome the drawbacks of LMS due to the instability of the algorithm in calculating the transfer function coefficient [28].

In this paper, two different ANC algorithms, i.e., LMS and NLMS are analyzed and implemented onto an FPGA-based EIT system in order to obtain higher accuracy of image reconstruction and the ADC performance parameters (the power spectral density (PSD) and the effective number of bits (ENOB)). The 2D reconstructed images quantitatively under experimental conditions in terms of amplitude response *AR*, position error *PE*, resolution *RES*, and shape deformation *SD* are also compared.

2. Implementation of Adaptive Noise Cancellation Algorithms

2.1 Architecture on FPGA-Based EIT System

Figure. 1 shows the proposed implementation of ANC algorithms on a field-programmable gate array (FPGA)-based electrical impedance tomography (EIT) system. FPGA-based EIT system is composed of a circular-shape sensor, multiplexer (MUX), signal conditioning, and FPGA. The circular-shape sensor composed of 32 electrodes is attached to a MUX in order to interchange the boundary condition of electrodes, whether as transmitter electrodes (V_{hc} and V_{lc}) or receiver electrodes (V_{hp} and V_{lp}). FPGA consists of a voltage generator, implemented ANC algorithms, and voltmeter. The transmitter electrodes


Figure 1. Adaptive filter implementation in FPGA-based EIT system.

(V_{hc} and V_{lc}) are connected to the constant current source (CCS-PI controlled) in order to maintain the constant current inside of the sensor. Meanwhile, the receiver electrodes are connected to ANC algorithms and voltmeter through an analog-to-digital converter (ADC). The ANC algorithms are connected to each receiver electrodes readout.

For each receiver electrodes readout, the converted analog data of $V_{hp}[k]$ or $V_{lp}[k]$ are the sensing signal at receiver electrodes $D_1[k]$ and $D_2[k]$. Practically, the sensing signal D_i contains noise signal h. Where i is the order number of signal. By using the filter tap weights vector W, the output signal Y_i can be calculated, which is the free-noise signal of sensing signal D_i. On this FP-

GA-Based EIT System, the input signal X is the output of the voltage generator. In order to calculate filter tap weights vector W_i, the error signal e_i should be maintained as low as possible which is given by the following relationship

(a)

(b)
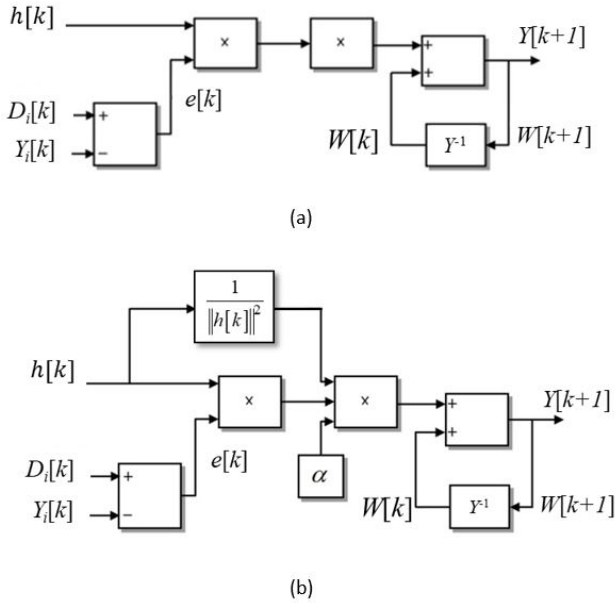
Figure 2. Scheme of an ANC algorithm: (a) block diagram of LMS algorithm, and (b) block diagram of NLMS algorithm

$$\mathbf{e}_i = \mathbf{D}_i - \mathbf{Y}_i \tag{1}$$

The calculation of the filter tap weights vector W itself varies among the proposed ANC algorithms. In this study, the two ANC algorithms are explained in the following sub-section.

2.2 Adaptive Noise Cancellation Algorithms

2.2.1 Least Mean Squares (LMS) Algorithm

In order to minimize the error signal e_i, LMS algorithm is based on a stochastic gradient algorithm that uses a gradient vector of the filter tap weight to converge on the optimal Wiener solution [29]. The block diagram of LMS algorithm within an ANC scheme is shown in Figure. 2(b). It should be noted that the sensing signal D_i induced by excitation voltage has a similar statistical property with the input signal X. Thus, generally, the sensing signal D_i can be expressed by a weighting transformation which applied on the input signal X. With the filter tap weights vector W, it is feasible to train the input signal X and finally obtain the best filtering result of the estimation of the desired signal Y_i. The estimation of the desired signal Y_i contains the noise

signal h as low as possible by implementing the filter tap weights vector W.

In order to achieve the optimal filtering, LMS adjust its filter parameters iteratively when the statistical properties of the sensing signal changes with the following equation [30]:

$$W[k+1] = W[k] + 2\mu e[k] X[k] \tag{2}$$

where, μ [-] is the step size parameter to control the speed of the LMS filter by using weight update for each iteration of ANC, and k is the number of iteration. In order to apply eq. (2) onto eq. (1), a structure of filter within the adaptive system employs a digital finite impulse response (FIR) filter in a time instant n [30].

$$Y_i[n] = \sum_{k=0}^{L-1} W_k[n] * X[n-k] = W^T[n] X[n] \tag{3}$$

$$X[n] = \left[x(n), x(n-1), \dots, x(n-L+1) \right]^T \tag{4}$$

$$W[n] = \left[w_n(0), w_n(1), \dots, w_n(L-1) \right]^T \tag{5}$$

Where, L_j is the filter length, and j is the value determined from the sequence 2^n of 2, 4, 8, 16, 32, 64, 128, 256, 512, 1024, 2048.

2.2.2 Normalized Least Mean Squares (NLMS) Algorithm

The NLMS algorithm, as shown in Figure 2(b) derived from LMS revises the characteristics of the step size parameter m [-] in order to solve the LMS filter drawback [31,32]. In NLMS filter, the filter tap weights $W[k+1]$ is normalized with the squared Euclidian norm of the noise signal $h[k]$ as the following equation:

$$W[k+1] = W[k] + \left(\frac{\alpha}{c + \left\| h[k] \right\|^2} \right) e[k] X[k] \tag{6}$$

where, α is the NLMS adaptation constant that optimizes the convergence rate of the NLMS filter, and its possible range is $0 < \alpha < 2$. c [-] is time-dependent filter coefficients which are the positive constant term and is always less than 1. In order to compute the norm of the noise signal h[k], eq. (7) is used as follows

$$\|h[k]\| = \sqrt{\sum |h[k]|^2} \tag{7}$$

In the case of the LMS algorithm, a proper value selection of the step size parameter m [-] is important to the performance of ANC. The lower value of step size parameter m [-], the longer time of LMS filter to converge on the optimal Wiener solution. However, the higher value of the step size parameter m [-], the LMS filter becomes unsteady and diverge. Moreover, the noise signal h amplitude is not steady during the change of time due to the instability of the input signal X that leads to the step size parameter m [-] varies in time and affects to the convergence rate [31,32]. In this regards, finding the best of the step size parameter m [-] of LMS is troublesome.

3. Experiments

3.1 Experimental Setup and Conditions

As shown in Figure.3, the experimental setup of an FPGA-based EIT system is composes of a high resolution and high speed ADC by implementing the Red-Pitaya platform which has a dual-port (14 bit DAC, 125 MSps) DAC1401D125 from NXP Semiconductors, a dual-ADC's (14 bit ADC, 125 MSps) LTC2145 from Linear Technology, and a FPGA-ZYNQ 7010 System on Chip (SoC) from Xilinx Co.Ltd. This FPGA is chosen because it has potentially sufficient for the implementation of a complete instrument with an ANC and a spectrum analyzer with a portable system. The input stage of FPGA-ZYNQ 7010 has been modified by inserting 1:1 RF balun as an isolation transformer, enabling the acquisition of signals up to 125 MHz in order to increase the bandwidth of measurement and to characterize the jitter effect [33]. This FPGA-based EIT system has 32-channels electrode with vessel diameter $d = 125$ mm. The 32-channel electrodes are attached on the active electrode circuit that converts the analog signal transmission between electrode and FPGA system into the digital signal.

In order to eliminate the need of constant current circuit, an artificial constant current source proportional-integral controlled (CCS-PI controlled) is used by implementing a PID controller inside of FPGA (see Figure.1 and Figure. 4(a)). This method could be possible because of the intensity of input signal X and the range resistance of R_{load} which is the electrical properties of an object interest are known priory. Figure. 4(b) shows the comparison of current I_{out} that injected onto the object of interest in the case of variant R_{load}. The result shows that constant current is stable until frequency 35 kHz.

3.2 Phantom Conditions
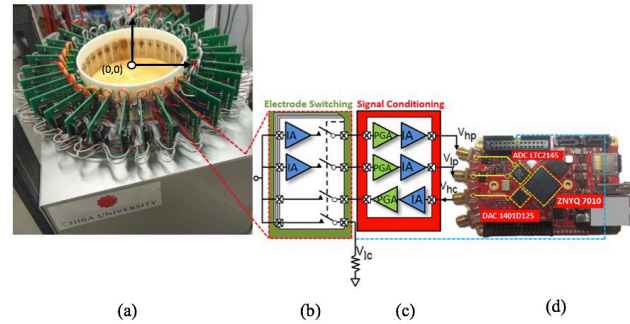
Figure 3. Manufactured of FPGA-based EIT system which consists of (a) 32 active electrodes attached to circular-shape vessel, (b) MUX-I or MUX-V (electrode switching), (c) Signal conditioning, and (d) FPGA system based on ZYNQ-7010

Two agar phantoms to demonstrate the feasibility of the proposed method were built based on NaCl powder (Wako, Osaka, Japan) and agar powder (Wako). Agar phantom-1 was composed of chicken meat with a diameter of $d_1 = 50$ mm and immersed in agar phantom background with conductivity $\sigma_b = 0.3$ S/m.
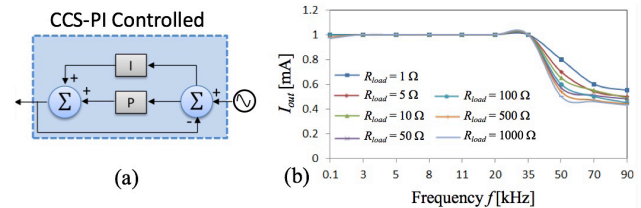
Figure 4. (a) Block diagram of constant current source PI controlled, and (b) constant current at frequency variant.

Agar phantom-2 was composed of one cylinder agar block inclusion with a diameter of $d_2 = 20$ mm and conductivity $s_i = 0.7$ S/m was immersed in agar phantom background with conductivity $\sigma_b = 0.3$ S/m. Image noise analysis is evaluated with input signal $X = 2$ V_{p-p} and five different positions of cylinder agar inclusions along the x-axis from right to left until the center of the conductive medium.

3.3 Image Reconstruction Evaluation Method

Five different positions of cylinder agar inclusions are investigated by using the image reconstruction performance parameters in EIDORS, which are amplitude response *AR*, position error *PE*, resolution *RES*, and shape deformation *SD* [34]. *AR* [-] indicates how the inclusion's amplitude contribute to the overall reconstructed image's amplitude by measuring the ratio of image pixel amplitudes between the normalized inclu-

sion's amplitude A_m [-] and the normalized area of inclusion A_{inN} [-]. m is the pixel matrix of the reconstructed image with resolution 64 x 64.

$$AR = \frac{\sum_m A_m}{A_{inN}} \qquad (8)$$

PE [-] indicates the accuracy of the reconstructed image in detecting the location of inclusion. r_t is the predicted center of the inclusion in the reconstructed image, while r_q is the actual location of the center of the inclusion in the phantoms.

$$PE = r_t - r_q \qquad (9)$$

RES [-] indicates the smallest visible object by calculating the ratio of inclusion's area A_{in} [mm^2] and total reconstructed image's area A_T [mm^2].

$$RES = \sqrt{A_{in} / A_T} \qquad (10)$$

SD [-] indicates the fraction of the outside area of inclusion A_c [mm^2] in the reconstructed image, which is not covered by the inclusion area A_{in} [mm^2]. A_{in} [mm^2] is the area of inclusion in the reconstructed image.

$$SD = \frac{A_c}{A_{in}} \qquad (11)$$

3.4 Experimental Results and Evaluation

Figure. 5 shows the comparison of reconstructed images of agar phantom-1 by using and without adaptive filter algorithms in the case of different input signal amplitude X = [X, X/2, X/3, X/5]. The ANC algorithms used Figure. 5 was NLMS. Without using the ANC algorithm on FPGA-based EIT system shows the inaccuracy of the reconstructed image as compared with using the ANC.

Figure. 6 shows the comparison of reconstructed images of agar phantom-2 based on LMS and NLMS algorithm implementation. It can be seen that the LMS filter algorithm is dominantly contributed by image noise from near the boundary position to the center position of object inclusion. Reconstructed images of NLMS is preferable from the inclusion, which is placed close to the electrodes to the center position. Although NLMS reconstructed images pattern has less tolerant to noise and a lower dynamic range, it performs better when the target is placed close to the electrodes. The image artifact on LMS and NLMS reconstructed images has increased slightly among the different inclusion.

The evaluation of reconstructed images is shown in Figure. 7. The reconstructed EIT images with NLMS is better than the images with LMS by amplitude response AR = 12.5%, position error PE = 200%, resolution RES = 33%, and shape deformation SD = 66%. The desired behavior of amplitude response AR is constant in the whole position inside the sensor. The reconstructed images of LMS and NLMS showed similar behavior in the case of AR. In the case of position error PE, reconstructed images of LMS have bigger PE as compared with NLMS. The instability of the sensing signal causes the higher PE of LMS, and it is indicated by high image noise as shown in Figure. 6. Meanwhile, in the case of resolution RES, the desired behavior is small and uniform. Both reconstructed images of LMS and NLMS showed similar behavior in the case of RES. Furthermore, this instability sensing signal can be quantified by using the shape deformation SD. As can be seen in the image reconstruction of LMS, it has high shape deformation. The value of shape deformation SD also indicates that the LMS filter algorithm is not properly filtered and still create image artifact in the reconstructed images.
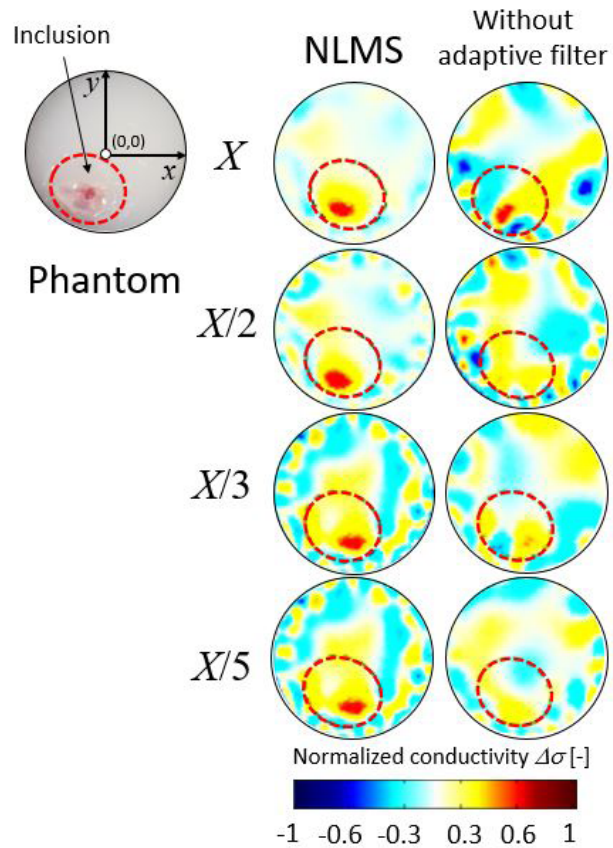

Figure 5. Comparison of reconstructed images between using and without adaptive filter.
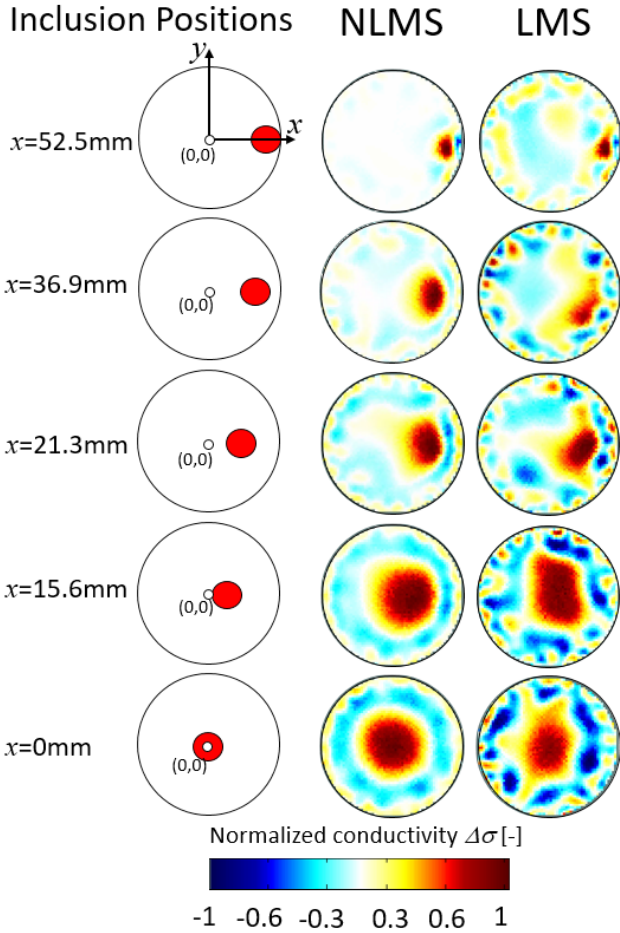
Figure 6. Comparison of reconstructed images.

Figure 7. Evaluation of image reconstruction performances: (a) amplitude response *AR*, (b) position error *PE*, (c) resolution *RES*, and (d) shape deformation *SD*.

Figure 8. Noise signal sources model on FPGA-based EIT system.

4. Discussion

4.1 Analysis Method and Condition

We discuss the analysis of ANC algorithms implemented onto FPGA-based EIT system in terms of the capability to reduce noise signal. Both phase and amplitude of sensing signals entering ADC $D_{0,i}[k]$ as shown in Figure.1 have affected by the noise signal as well as input signal leaving DAC $X[k]$. The noise signal sources in FPGA-based EIT system as shown in Figure. 8 consists of the input signal noise $g[k]$, the sample-and-hold (S/H) noise $r[k]$, the voltage reference noise $b[k]$, and the quantizer noise $q[k]$. Based on the dependent response of the input signal variance, the performance of ANC algorithms was investigated.
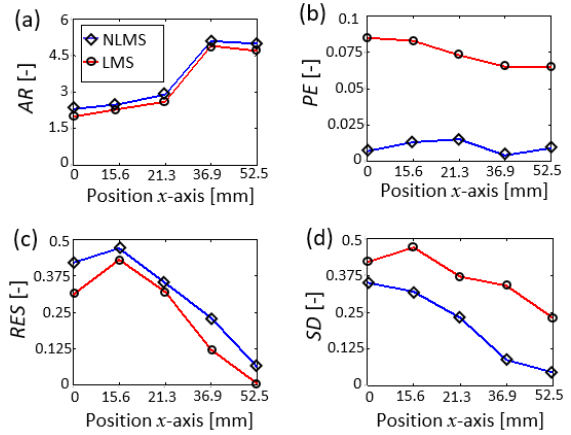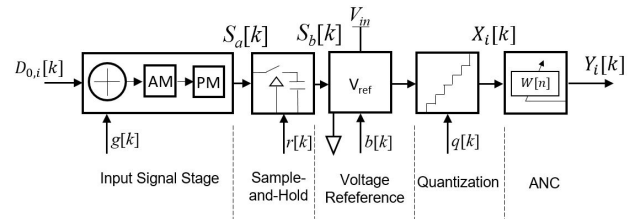
The input signal noise $g[k]$ of an ADC behaves as an additive white noise [35], [36] which mainly affects the amplitude sensing signal. The additive white noise is caused by such as a thermal, and circuit node noise. The contribution of additive white noise can be expressed by

$$s_a[k] = D_{0,i}[k] + g[k] \tag{12}$$

The sample-and-hold (S/H) noise $r[k]$ or aperture jitter affects mainly on the phase sensing signal. Time fluctuations occur in ADC's sample-and-hold which generate a parametric noise. Time fluctuations are also known as aperture jitter which is defined as the variation of the sampling instant at a time kt. Hence, the effect of aperture jitter can be described as follows

$$s_b[k] = s_a\left(kt + r[kt]\right) \tag{13}$$

At this stage, $s_b[k]$ is converted into digital form, as described in eq. (15), where m is the resolution of the ADC, V_{ref} is the voltage reference, and $q[k]$ is the quantization noise:

$$s_c[k] = s_b[k]\frac{2^m}{V_{ref}} + q[k] \tag{14}$$

At the voltage reference stage, the voltage reference noise $b[k]$ caused by a non-ideal source from instability voltage over temperature and time. The voltage reference noise $b[k]$ is described as a non-ideal source, $V_{ref} = V_{rb}$ $(1+b[k])$. Here, V_{rb} is the nominal value. This noise behaves as a parametric noise that the character noise depends on the voltage reference topology [37]. Differential amplifier equation is to solve the constant values of m and V_{rb}. The voltage reference noise as a reference in input ADC can divide the ADC output by $2^m/V_{ref}$. Hence, ADC output is expressed as

$$s_d[k] = s_c[k] \frac{v_{rb}}{2^m} \tag{15}$$

Lastly, the ADC output is stated in terms of the additive and parametric noise are described by

$$X_i[k] = \Big(g[k] + s_b\big(kt + (r[k])\big)\Big)\big(1 + b[k]\big) \tag{16}$$

The voltage reference noise is considered $b[k] \ll 1$.

Considering the noise signal sources as aforementioned, thus we can analyze how this noise signal sources affect the amplitude and phase sensing signal by the following mathematical relationship

$$PN = \frac{1}{V_0} g[k] + 2\pi V_0 r[k] \tag{17}$$

Where $1/V_0$ is normalization of amplitude fluctuation generated by input signal noise and summing using the conversion of aperture jitter $2\pi V_0 r[k]$ false from analog to digital converter. The unity of PN is radian. Meanwhile, the amplitude signal noise AN is also generated by input signal noise, but with a difference summation that is induced by voltage reference noise $b[k]$:

$$AN = \frac{1}{V_0} g[k] + b[k] \tag{18}$$

The AN is a non-dimensional. Then, the phase and amplitude signal noise can be fitted by polynomial law to compute the power spectrum density:

$$S_Q[f] = \frac{1}{V_0^2} S_g[f] + 4\pi^2 V_0^2 s_r[f] \tag{19}$$

$$S_I[f] = \frac{1}{V_0^2} S_g[f] + S_b[f] \tag{20}$$

Thus, the PSD of phase signal noise $S_Q[f]$ and ampli-

tude signal noise $S_I[f]$ can be calculated by Eq. (19) and Eq. (20) respectively. In this PSD of amplitude and phase signal noise, the contribution of each noise signal sources is identified as a complete description of the device limitations.

4.2 Analysis Results

We realize that the readout of the estimation of the output signal Y_i is available at a single frequency signal. Because the impedance measurements are a sweep frequency measurement, we need to confirm the free noise of sensing signal D_i at the readout of the voltmeter in the spectral region. In this regards, we need to apply the power spectral density PSD analysis. The ANC algorithms of LMS and NLMS are supposed to suppress the noise signal h_i in order to obtain the estimation of the output signal Y_i without the drawbacks from the noise signal. The LMS and NLMS are evaluated through PSD analysis by comparing with PSD of noise signal floor NF. As shown in Figure. 9, the PSD of NF is $NF = -164$ dBV^2/Hz in the case of ADC 14 bit, primary signal $X = 2$ V$_{p-p}$, and the step size parameter $\mu = 0.002$ [-]. As closer the PSD of the desired signal to PSD of NF, it indicates as better ANC algorithms performance.
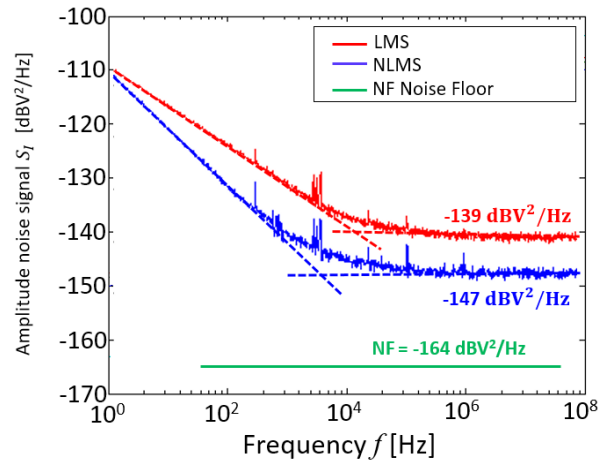
Figure 9. Comparison of PSD of amplitude sensing signal S_I between NLMS, LMS, and Noise floor in the case of phantom as shown in Figure 5

The spectrum analysis of four noise sources has been considered as a common noise of two ADC of receiver electrodes, as shown in Figure. 8. The output of ADC was synchronously sampled by one sample every one signal period in order to measure the influence of noise signals. The sensing signal D_i which is the output of ADC has affected by the noise signal can be analyzed in terms of amplitude and phase signal which were detected by using two points of a cosine wave of $u_i[k]$. These points consist

of zero-crossing detection and voltage peak detection. Zero crossing detection is related to phase signal noise *PN*, the measurement of *PN* results in the prediction of the phase noise generated by quadrature noise. Voltage peak detection is related to amplitude signal noise *AN*, the measurement of *AN* result in the prediction of the amplitude noise generated by in-phase noise.

Some of the important ADC performance parameters are signal-to-noise ratio *SNR*, signal-to-noise and distortion ratio *SNDR*, effective number of bits *ENOB*, spur free dynamic range *SFDR*, total harmonic distortion *THD*, inter modulation distortion *IMD* and effective resolution bandwidth *ERBW* [38]. Among these ADC performance parameters, *ENOB* reflects the resolution and the accuracy of an ideal ADC circuit under consideration in dynamic measurement that is suitable for high sensitivity detection analysis in most EIT applications [39,40].

The contribution of ANC performance increases *ENOB* performance, and it directly related to SNR measurement. The Analog-to-Digital Converter (ADC) performances of PSD and the effective number of bit *ENOB* with NLMS is higher than the performances with LMS by S_I = 5.7 % and *ENOB* = 15.4 %. Therefore, high image noise in the LMS adaptive filter indicates the voltage signal with low SNR. Figure. 8 shows the PSD of the voltage noise with LMS and NLMS algorithm that it can be obtained by connecting the combination of two ADC inputs to ground through a 50 Ω resistor (X = 2 V$_{p-p}$, f_s = 125 MHz). This noise corresponds to the amplitude noise induced by the input stage that contains signal instability. As shown in Table I when LMS is applied to the system, it presents an additive white noise of S_I = -139 dBV^2/Hz. Meanwhile, NLMS shows better performance in term of the additive white noise value. The additive white noise value of NLMS is S_I = -147 dBV^2/Hz. This additive white noise close to the quantization of noise floor *NF* = -164 dBV^2/Hz. From PSD plot of additive white noise, the level of additive white noise is also described for actual *ENOB* value of ADC. The actual *ENOB* of LMS algorithm is *ENOB* = 9.7 bit. Meanwhile, the actual *ENOB* of NLMS algorithm increases to *ENOB* = 11.2 bit.

Table 1. Comparison of ANC algorithms performance

ANC	*ENOB*	S_I
LMS	9.7 bit	-139 dBV^2/Hz
NLMS	11.2 bit	-147 dBV^2/Hz

Figure. 10(a) and (b) show the comparison of the capability to reduce noise signal between LMS and NLMS in terms of PSD analysis of phase signal noise PN = S$_Q$ [dBrad^2/Hz]. While Figure. 11(a) and (b) show the com-parison of PSD of amplitude signal noise *AN* = S_I [dB/Hz]. Four voltage levels of input signal X, X = 2 V$_{p-p}$ to X/5 = 0.4 V$_{p-p}$, were used to investigate the PSD level in order to compare the performance between LMS and NLMS.

As shown in Figure. 10(a) and (b), phase signal noise *PN* are dominated by the additive noise of the input stage, although the aperture jitter also occurs. Furthermore, it increases proportionally to the input amplitude variance $1/V_0^2$. As it can be seen that under this condition, *PN* is dependent on the input amplitude variance $1/V_0^2$. Additive flicker and additive white noise of NLMS at each input amplitude level are higher than LMS.

The PSD of amplitude signal noise S_I produces the same result that NLMS has higher PSD level as compared with LMS as shown in Figure. 10(a) and (b). In terms *AN*, the influence of additive noise by harmonic contributions of the signal generator is dominant. The PSD analysis results of *PN* and *AN* are appropriate with the noise model, as shown in Eq. (19) and (20). Finally, the capability of reducing the noise of NLMS contributes to increasing the accuracy of the reconstructed image is shown in Figure. 6 and increasing the *ENOB* that reflects the high sensitivity detection of FPGA-based EIT system as shown in Table 1.
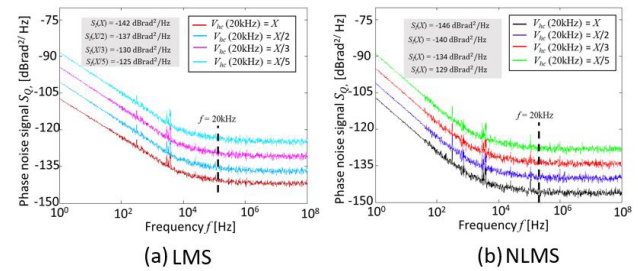
Figure 10. PSD of phase sensing signal of (a) LMS and (b) NLMS in the case homogenous agar condition.
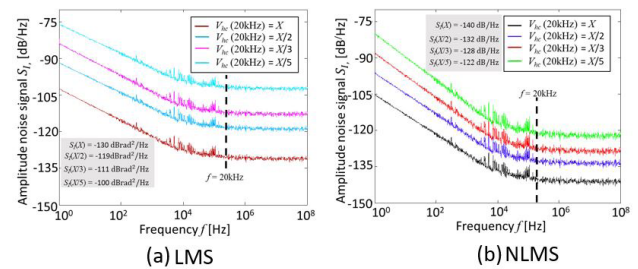
Figure 11. PSD of amplitude sensing signal of (a) LMS and (b) NLMS in the case homogenous agar condition.

5. Conclusion

In this paper, we proposed the implementation of adaptive noise cancellation (ANC) algorithms, i.e. least means square (LMS) and normalized least means square (NLMS) algorithm, for FPGA-based EIT system in order to elimi-

nate the noise signal and to increase the sensitivity detection by increasing the effective number of bit (*ENOB*) of ADC parameter. This study evaluates the benefit of ANC algorithms application on the new field which is the Electrical Impedance Tomography (EIT) system. The ANC of LMS and NLMS algorithm work by calculating the transfer function coefficients in order to minimize the error signal between the sensing signal D_i and the noise signal h itself. The ANC of LMS and NLMS algorithm was compared and evaluated through experimental studies.

The experimental results showed that the implementation of ANC algorithms onto FPGA-based EIT system:

(1) Implementing ANC algorithms on FPGA-based EIT system shows significantly more accurate image reconstruction to show the inclusion as compared without ANC algorithms implementation.

(2) ADC performances of NLMS has S_I = -147 dBV^2/Hz and effective number of bit (*ENOB*) = 11.2 bit.

(3) ADC performances of LMS has S_I = -139 dBV^2/Hz and *ENOB* = 9 bit.

Higher ADC performances of NLMS as compared with LMS leads to the better image reconstruction performances in terms of amplitude response (*AR*), position error (*PE*), resolution (*RES*), and shape deformation (*SD*).

We realize that several ANC algorithms are already proposed, not only LMS or NLMS. On this regards, this consideration opens a new opportunity to apply the variant of ANC algorithms that could be suitable with different EIT applications.

Acknowledgment

References

[1] X. Liu, J. Yao, T. Zhao, H. Obara, Y. Cui, and M. Takei. Image Reconstruction Under Contact Impedance Effect in Micro Electrical Impedance Tomography Sensors. IEEE Trans. Biomed. Circuits Syst., 2018,12(3): 623-631
DOI: 10.1109/TBCAS.2018.2816946

[2] A. Sapkota, T. Fuse, M. Seki, O. Maruyama, M. Sugawara, and M. Takei. Application of electrical resistance tomography for thrombus visualization in blood. Flow Meas Instrum., 2015, 46: 334–340.
DOI: 10.1016/j.flowmeasinst

[3] B. S. Kim, A. K. Khambampati, Y. J. Hong, S. Kim, and K. Y. Kim. Multiphase flow imaging using an adaptive multi-threshold technique in electrical resistance tomography. Flow Meas. Instrum., 2013, 31: 25–34.
DOI: 10.1016/j.flowmeasinst.2012.11.003

[4] Z. Wang, T. Zhao, and M. Takei. Morphological Structure Characterizations in Lithium-Ion Battery (LIB) Slurry under Shear Rotational Conditions by On-Line Dynamic Electrochemical Impedance Spectroscopy (EIS) Method. J. Electrochem. Soc., 2017, 164(9): A2268–A2276.
DOI: 10.1149/2.0391712jes

[5] A. McEwan, G. Cusick, and D. S. Holder. A review of errors in multi-frequency EIT instrumentation. Physiol. Meas., 2007, 8(7): S197-215.
DOI: 10.1088/0967-3334/28/7/S15

[6] J. Rosell, D. Murphy, R. Pallas, and P. Rolfe. Analysis and assessment of errors in a parallel data acquisition system for electrical impedance tomography. Clin. Phys. Physiol. Meas., 1988, 9(4A): 93–99.
DOI: 10.1088/0143-0815/9/4A/016

[7] M. Rafiei-Naeini and H. McCann. Low-noise current excitation sub-system for medical EIT. Physiol. Meas., 2008, 29(6): S173–S184.
DOI: 10.1088/0967-3334/29/6/S15

[8] M. Yasin, S. Böhm, P. O. Gaggero, and A. Adler. Evaluation of EIT system performance. Physiol. Meas., 2011, 32(7): 851.

[9] M. R. Baidillah, A.-A. S. Iman, Y. Sun, and M. Takei. Electrical Impedance Spectro-Tomography based on Dielectric Relaxation Model. IEEE Sens. J., 2017, 17(24): 8251–8262.
DOI: 10.1109/JSEN.2017.2710146

[10] R. W. M. Smith, I. L. Freeston, B. H. Brown, and A. M. Sinton, "Design of a phase-sensitive detector to maximize signal-to-noise ratio in the presence of Gaussian wideband noise," Meas. Sci. Technol., 1992, 3(11): 1054–1062.
DOI: 10.1088/0957-0233/3/11/006

[11] N. Liu, G. J. Saulnier, and J. C. Newell. A multi-channel synthesizer and voltmeter for electrical impedance tomography. in Proceedings of the 25th Annual International Conference of the IEEE Engineering in Medicine and Biology Society (IEEE Cat. No.03CH37439), 2003: 3110–3113.
DOI: 10.1109/IEMBS.2003.1280800

[12] E. K. Murphy, M. Takhti, J. Skinner, R. J. Halter, and K. Odame. Signal-to-Noise Ratio Analysis of a Phase-Sensitive Voltmeter for Electrical Impedance Tomography. IEEE Trans. Biomed. Circuits Syst., 2017, 11(2): 360–369.
DOI: 10.1109/TBCAS.2016.2601692

[13] J. Yao and M. Takei. Application of Process Tomography to Multiphase Flow Measurement in Industrial and Biomedical Fields: A Review. IEEE Sens. J., 2017, 17(24): 8196–8205
DOI: 10.1109/JSEN.2017.2682929

[14] R. J. Halter, A. Hartov, and K. D. Paulsen. A Broadband High-Frequency Electrical Impedance Tomography System for Breast Imaging. IEEE Trans. Biomed. Eng., 2008, 55(2): 650–659.
DOI: 10.1109/TBME.2007.903516

[15] C. Brady, J. Arbona, I. S. Ahn, and Y. Lu. FPGA-based adaptive noise cancellation for ultrasonic NDE application. in 2012 IEEE International Conference on Electro/Information Technology, 2012: 1–5.
DOI: 10.1109/EIT.2012.6220729

[16] A. Rosado-Munoz, M. Bataller-Mompean, E. Soria-Olivas, C. Scarante, and J. F. Guerrero-Martinez. FPGA Implementation of an Adaptive Filter Robust to Impulsive Noise: Two Approaches. IEEE Trans. Ind. Electron., 2011, 58(3) 860–870.
DOI: 10.1109/TIE.2009.2023641

[17] R. Kusche, A. Malhotra, M. Ryschka, G. Ardelt, P. Klimach, and S. Kaufmann. A FPGA-Based Broadband EIT System for Complex Bioimpedance Measurements—Design and Performance Estimation. Electronics, , 2015, 4(3): 507–525.
DOI: 10.3390/electronics4030507

[18] Z. Xu et al.. Development of a Portable Electrical Impedance Tomography System for Biomedical Applications. IEEE Sens. J., 2018, 18(19): 8117–8124.
DOI: 10.1109/JSEN.2018.2864539

[19] X. Yang, Y. Xu, and F. Dong. A FPGA-based multi-frequency current source for biological EIT system. Conf. Rec. - IEEE Instrum. Meas. Technol. Conf., 2016, 2016(61302122): 1–6.
DOI: 10.1109/I2MTC.2016.7520538

[20] G. Kou and L. Rong. FPGA-based digital phase-sensitive demodulator for EIT system. 2007 8th Int. Conf. Electron. Meas. Instruments, ICEMI, 2007: 4845–4848.
DOI: 10.1109/ICEMI.2007.4351274

[21] S. A. Santos, A. Robens, A. Boehm, S. Leonhardt, and D. Teichmann. System description and first application of an FPGA-based simultaneous multi-frequency electrical impedance tomography. Sensors (Switzerland), 2016, 16(8).
DOI: 10.3390/s16081158

[22] X. Yue and C. McLeod. FPGA design and implementation for EIT data acquisition. Physiol. Meas., 2008.
DOI: 10.1088/0967-3334/29/10/007

[23] M. R. Naeini and H. McCann. A High Performance, Space Effective FPGA-Based Signal Generation and Measurement System for Medical EIT. in World Congress on Medical Physics and Biomedical Engineering 2006. IFMBE Proceedings, vol. 14, R. Magjarevic and J. H. Nagel, Eds. Springer, Berlin, Heidelberg, 2006: 3878–3881.
DOI: https://doi.org/10.1007/978-3-540-36841-0_981

[24] Chang-Min Kim, Hyung-Min Park, Taesu Kim, Yoon-Kyung Choi, and Soo-Young Lee, "FPGA implementation of ICA algorithm for blind signal separation and adaptive noise canceling," IEEE Trans. Neural Networks, 2003, 14(5): 1038–1046.
DOI:10.1109/TNN.2003.818381

[25] A. Di Stefano, A. Scaglione, and C. Giaconia. Efficient FPGA Implementation of an Adaptive Noise Canceller. in Seventh International Workshop on Computer Architecture for Machine Perception (CAMP'05), 2005: 87–89.
DOI: 10.1109/CAMP.2005.22

[26] T. Lan and J. Zhang. FPGA Implementation of an Adaptive Noise Canceller. in 2008 International Symposiums on Information Processing, 2008: 553–558.
DOI: 10.1109/ISIP.2008.107

[27] B. Widrow et al.. Adaptive noise cancelling: Principles and applications. Proc. IEEE, 1975, 63(12): 1692–1716.
DOI: 10.1109/PROC.1975.10036

[28] J. Nagumo and A. Noda. A learning method for system identification. IEEE Trans. Automat. Contr., 1967, 12(3): 282–287.
DOI: 10.1109/TAC.1967.1098599

[29] B. Widrow and M. Hoff. Adaptive switching circuits. IRE WESCON Conv. Rec., 1960, 4: 96–104.
DOI: 10.1088/0264-9381/23/9/024

[30] K. Mayyas. Performance analysis of the deficient length LMS adaptive algorithm. IEEE Trans. Signal Process., 2005, 53(8): 2727–2734.
DOI: 10.1109/TSP.2005.850347

[31] H. C. So. Modified LMS algorithm for unbiased impulse response estimation in nonstationary noise. Electron. Lett., 1999, 35(10): 791.
DOI: 10.1049/el:19990523

[32] S. Gazor. Prediction in LMS-type adaptive algorithms for smoothly time varying environments. IEEE Trans. Signal Process., 1999, 47(6): 1735–1739.
DOI: 10.1109/78.765152

[33] A. Devices Inc, LTC2145-14 Datasheet, 2018. [Online]. Available:
http://www.analog.com/en/products/analog-to-digital-converters/standard-adc/high-speed-ad-10msps/

ltc2145-14.html#product-overview [Accessed: 25-Jun-2018].

[34] A. Adler et al. GREIT: a unified approach to 2D linear EIT reconstruction of lung images. Physiol. Meas. Physiol. Meas, 2009, 30(30): 35–55. DOI: 10.1088/0967-3334/30/6/S03

[35] L. Fabrizi, A. McEwan, E. Woo, and D. S. Holder. Analysis of resting noise characteristics of three EIT systems in order to compare suitability for time difference imaging with scalp electrodes during epileptic seizures. Physiol. Meas., 2007, 28(7): S217–S236. DOI: 10.1088/0967-3334/28/7/S16

[36] A. R. Frangi, P. J. Riu, J. Rosell, and M. A. Viergever. Propagation of measurement noise through back-projection reconstruction in electrical impedance tomography. IEEE Trans. Med. Imaging, 2002, 21(6): 566–578.

DOI: 10.1109/TMI.2002.800612

[37] M. Oljaca and B. Baker. How the voltage reference affects ADC performance, Part 2. Analog Appl. J., 2009, 3Q: 13–16.

[38] M. Figureueiredo, J. Goes, and G. Evans, Reference-Free CMOS Pipeline Analog-to-Digital Converters. New York, USA: Springer-Verlag, 2013. DOI: 10.1007/978-1-4614-3467-2

[39] J. J. Blair and T. E. Linnenbrink. Corrected rms error and effective number of bits for sine wave ADC tests. Comput. Stand. Interfaces, 2004, 26(1): 43–49. DOI: 10.1016/S0920-5489(03)00061-8

[40] D. Belega, D. Dallet, and D. Petri. A High-Performance Procedure for Effective Number of Bits Estimation in Analog-to-Digital Converters. IEEE Trans. Instrum. Meas., 2011, 60(5): 1522–1532. DOI: 10.1109/TIM.2010.2089151